Synthesis and structure of ruthenium-fullerides

Faqiang Leng, I.C. Gerber, Pierre Lecante, Wolfgang Bacsa, J. Miller, J.R. Gallagher, S. Moldovan, M. Girleanu, M.R. Axet, Philippe Serp

RSC Advances

PAPER

View Article Online
View Journal | View Issue

Cite this: RSC Adv., 2016, 6, 69135

Synthesis and structure of ruthenium-fullerides†

F. Leng,[ab] I. C. Gerber,[c] P. Lecante,[d] W. Bacsa,[d] J. Miller,[e] J. R. Gallagher,[e] S. Moldovan,[f] M. Girleanu,[fg] M. R. Axet*[ab] and P. Serp*[ab]

Received 9th May 2016
Accepted 14th July 2016

DOI: 10.1039/c6ra12023g

www.rsc.org/advances

We report a simple and original procedure for preparing Ru–C_{60} polymeric chains, which spontaneously self-assemble as polymeric spherical particles. The size of the particles can be controlled by the choice of the solvent used during the reaction. In addition, these Ru–C_{60} polymeric spheres can be surface decorated with Ru nanoparticles using the same mild reaction conditions by changing the Ru/C_{60} ratio. Several techniques (TEM in high resolution, scanning and electron tomography modes, IR, NMR, Raman, WAXS, EXAFS and XPS) together with theoretical calculations allowed us to have an insight into the structure of these Ru–C_{60} species.

1. Introduction

Extensive investigations of fullerene C_{60}, both in its pristine form as well as in its doped or intercalated variants, have definitively confirmed a strong tendency toward polymerization of this molecule.[1] The combination of C_{60} and metals offer exciting perspectives for the production of novel fullerene-based architectures with unprecedented properties for catalysis,[2–4] batteries,[5] sensors[6] or nanoelectronic devices.[7] Indeed, the spherical shape, high degree of symmetry, and coordinating geometries of C_{60} make it an ideal candidate for the construction of well-defined supramolecular architectures. The metal fullerides have been the subject of intensive investigations over the past 20 years, and mostly compounds of C_{60} with alkali and alkaline metals (A-C_{60}) have been synthesized.[8] Metals in these compounds usually occupy interstitial sites in the octahedral or tetrahedral environment of the C_{60} structure. The bonding in these fullerides is ionic and the C_{60} molecules rotate freely. Li_4C_{60}, one of the most characteristic representatives of lithium intercalated fullerides, features an unusual type of two-dimensional polymerization.[9] In contrast, only a few reports claiming the existence of fullerides with transition metals (TM) are known;[10] and despite the progress in study of A-C_{60} polymerization,[11,12] the knowledge about this phenomenon in the TM–C_{60} systems is scarce. Transition metal fullerides can be prepared by chemical reactions in solution between a suitable TM complex and C_{60},[13] through electrochemical reduction from solutions of C_{60} and selected TM complexes,[14] or by co-evaporation of TM and C_{60} from separate sources under ultra-high vacuum (UHV) conditions.[15] Up to now, TM fullerides of Pd,[13] Pt,[16] Co,[17] Ru,[18] Fe,[19] Rh,[20] and Ti[15] have been reported. Although an understanding of the structure and bonding of the proposed compounds is highly desirable, the structure of these phases is still under discussion due to the poor crystallinity of the obtained samples. Depending on the amount of metal the suggested structure could be polymeric with a chain-like, two- or three-dimensional coordination. Moreover, it is believed that metal atoms serve as bridges connecting neighboring C_{60} molecules.

The first and the most studied, TM fulleride, Pd_x–C_{60}, was reported in 1992 by Nagashima *et al.*[13] This compounds, insoluble in most organic solvents, precipitated by mixing [$Pd_2(dba)_3$] (dba = dibenzylideneacetone) and C_{60} benzene solutions at room temperature. Two and three-dimensional amorphous polymeric structures were already proposed based on the results of electron probe microanalysis for Pd_x–C_{60}, but the exact nature of these polymers remains really unclear. Additionally, various TEM studies on the Pd_x–C_{60} compound suggest the possible presence of Pd nanoparticles (NPs) in the material.[21–23] The presence of metallic clusters was also evidenced for Ru_x–C_{60} compounds produced at higher temperatures from [$Ru_3(CO)_{12}$].[18,24] However, using TEM, Lavrentiev *et al.* have observed the polymeric chains in the Co_x–C_{60} mixture, which inner structure has been evaluated as (–C_{60}–Co–C_{60}–) order.[25] It is worth mentioning that most of these structural studies have used a single characterization techniques

[a]CNRS, LCC (Laboratoire de Chimie de Coordination), Composante ENSIACET, 4 allée Emile Monso, BP 44099, F-31030 Toulouse Cedex 4, France. E-mail: philippe.serp@ensiacet.fr; rosa.axet@lcc-toulouse.fr

[b]Université de Toulouse, UPS, INPT, F-31077 Toulouse Cedex 4, France

[c]Université de Toulouse, INSA, UPS, CNRS, LPCNO (IRSAMC), 135 avenue de Rangueil, F-31077 Toulouse, France

[d]Centre d'élaboration des Matériaux et d'études Structurales UPR CNRS 8011, 29 Rue Jeanne-Marvig, BP 4347, 31055 Toulouse, France

[e]Argonne National Laboratory, Chemical Sciences and Engineering Division, 9700 S. Cass Ave, Building 200, Argonne, IL 60429-4837, USA

[f]Institut de Physique et Chimie des Matériaux de Strasbourg, UMR 7504 CNRS-UdS, 23 rue du Loess BP43, 67034 Strasbourg Cedex 2, France

[g]Institut de Recherche Biomédicales des Armées, Unité Imagerie, Place du Médecin Général Inspecteur Valérie André, BP73, 91220 Brétigny-sur-Orge, France

† Electronic supplementary information (ESI) available. See DOI: 10.1039/c6ra12023g

such as Raman spectroscopy,[19] XPS,[15] or TEM.[21] Some theoretical works, using Density Functional Theory (DFT), on exohedral fullerenes have been mainly devoted to the interaction between C_{60} and alkali atoms: Na, K,[26–29] and in a lesser extent TM, mainly V,[30] Ni,[31] Au[32,33] and Ta[34,35] and more recently with Pd and Pt atoms.[36] To our knowledge, no theoretical studies on the existence or the possible structures of $-C_{60}-TM-C_{60}-$ linear chains have been reported.

Considering the possible applications of these supramolecular architectures, it is important to have a better knowledge of their structure for the establishment of structure/properties relationships. In this context, we decided to reexamine the structure of such compounds in the case of ruthenium with a large variety of complementary characterization techniques, including TEM in high resolution, scanning and electron tomography modes, IR, NMR, Raman, WAXS, EXAFS and XPS, as well as DFT calculations. The combination of all these techniques allowed us to propose that $-C_{60}-Ru-C_{60}-$ polymers are formed and that Ru exhibits a $\eta^{2(6)}-\eta^6$ coordination mode. In addition, the control of the reaction conditions allows us to synthesize $C_{60}-Ru-C_{60}-$ polymers, nanospherical $Ru-C_{60}$ polymers, Ru Nps decorated nanospherical $Ru-C_{60}$ polymers, and Ru nanoparticles supported on a C_{60} matrix.

2. Experimental section

2.1 General methods

All operations were carried out under argon atmosphere using standard Schlenk techniques or in an MBraun glovebox. Solvents were purified by standard methods or by an MBraun SPS-800 solvent purification system. [Ru(COD)(COT)] was purchased from Nanomeps Toulouse, fullerene C_{60} from Sigma-Aldrich, CO and H_2 from Air Liquide. All these reactants were used as received.

The ruthenium content was established by inductively coupled plasma optical emission spectroscopy (ICP-OES) in a Thermo Scientific ICAP 6300 instrument. Solid state NMR (MAS-NMR) with and without $^1H-^{13}C$ cross polarization (CP) were performed on a Bruker Avance 400WB instrument equipped with a 4 mm probe with the sample rotation frequency being set at 12 kHz unless otherwise indicated. Measurements were carried out in a 4 mm ZrO_2 rotor. ATR-IR spectra were recorded on a Perkin-Elmer GX2000 spectrometer available in a glovebox, in the range 4000–400 cm^{-1}. The Raman spectra have been recorded with a Explora (Horiba) spectrometer in backscattering geometry using an optical objective $\times 100$ (NA 0.9). The wavelength of the incident laser has been 532 nm and the laser power was set to 1 mW.

2.2 TEM analyses

Some TEM and HRTEM analyses were performed by using a JEOL JEM 1011 CX-T electron microscope operating at 100 kV with a point resolution of 4.5 Å and a JEOL JEM 1400 electron microscope operating at 120 kV. The high resolution analyses were conduct using a JEOL JEM 2100F equipped with a Field Emission Gun (FEG) operating at 200 kV with a point resolution of 2.3 Å and a JEOL JEM-ARM200F Cold FEG operating at 200 kV with a point resolution of >1.9 Å. The approximation of the particles mean size was made through a manual analysis of enlarged micrographs by measuring at least 200 particles on a given grid. Other TEM micrographs were acquired with a JEOL 2100F S/TEM microscope equipped with a FEG operating at 200 kV, a spherical aberration probe corrector and a GATAN Tridiem energy filter. The resolutions attained are 2 Å and 1.1 Å under parallel TEM mode and scanning STEM modes, respectively. For STEM-HAADF analyses the spot size was of 0.13 nm, a current density of 140 pA, the camera focal length was 10 cm, corresponding to inner and outer detection angle of the annular detector of about 60 mrad and 160 mrad. For tomography experiments, the acquisitions of the tilt images series were performed using a high tilt sample holder, under angles spanning from +72 to -72°, with projections taken every 2° according to Saxton scheme. The irradiation damage was limited by using low electron doses. The images were first roughly aligned using a cross-correlation algorithm. A refinement of this initial alignment and a precise determination of the tilt axis direction were then obtained using the IMOD software where the centers of several Au nanoparticles from the analyzed group were used as fiducial markers.[37] The volume reconstructions have been computed using an iterative approach consisting of a simultaneous algebraic reconstruction technique implemented using the TOMO3D software,[38] the number of iterations not exceeding 40. Visualization and quantitative analysis of the final volumes were carried out using ImageJ software.

2.3 DFT calculations

DFT calculations were carried out using the Vienna ab initio simulation package VASP.[39–42] The code uses the full-potential projector augmented wave (PAW) framework.[43,44] Exchange-correlation effects have been approximated using the PBE functional[45] and applied in spin-polarized calculations. Besides to correctly describe weak intermolecular forces between $Ru-C_{60}$ complexes and solvent molecules, we have also used the optB86b-vdW functional.[46–49] We have checked that this scheme provide accurate geometries when van der Waals forces are the major bonding origin, as for instance in the C_{60} crystalline phase. See ESI.15† for the direct comparison between simulated and experimental WAXS spectra. If a slight compression factor of 1.5% is applied on the DFT structure, the agreement becomes almost perfect between peaks up to 0.8 nm. A kinetic-energy cutoff of 400 eV was found to be sufficient to achieve a total-energy convergence within several meV, considering a *k*-point sampling with a $(1 \times 1 \times 5)$ grid for the polymeric state or gamma-point only calculations for isolated molecules and complexes, in conjunction with a Gaussian smearing with a width of 0.05 eV. During geometry optimization runs and cell relaxations, all the atoms were fully relaxed until forces on individual atoms were smaller than 0.01 eV $Å^{-1}$. Calculation cells for isolated molecules and complexes were $25 \times 26 \times 27$ Å, to avoid spurious interactions between periodic images, when the same lattice parameters on (Ox) and (Oy) were kept fixed for the polymeric phase. Figures of the different geometries were produced thanks to the 3D visualization program VESTA.[50]

2.4 WAXS, EXAFS, and XPS analyses

Wide angle X-ray scattering measurements were performed on a diffractometer dedicated to Pair Distribution Function (PDF) analysis: graphite-monochromatized molybdenum radiation (0.07169 nm), solid state detection and low background setup. Samples were sealed in Lindemann glass capillaries (diameter 1.5 mm) to avoid any oxidation after filling in a glove box. For all samples data were collected on an extended angular range (129 degrees in 2 theta) with counting times of typically 150 s for each of the 457 data points, thus allowing for PDF analysis. Classic corrections (polarization and absorption in cylindrical geometry) were applied before reduction and Fourier transform.

X-ray absorption measurements were made on the bending magnet beam line of the Materials Research Collaborative Access Team (MRCAT) at the Advanced Photon Source, Argonne National Laboratory. The data were collected in step-scan, transmission mode. The 3 pre-edge regions, from −250 to −50 eV, −50 to −10 eV and −10 to 30 eV, were scanned in 10, 5 and 0.4 eV steps, respectively. The EXAFS was also scanned in 3 regions, to 6, from 6–10 and from 10–13 $Å^{-1}$. The data acquisition time in each region was increased to give a high signal to noise in the k^2-weighted chi. The Ru on C_{60} samples were handled and loaded in the absence of air and water in a glove box. The samples were placed in an environmental cell for data acquisition. The samples were additionally treated in 4% H_2/He at 150 °C, cooled to room temperature and data taken without exposure to air. A ruthenium foil spectrum was acquired simultaneously with each measurement for energy calibration. Samples were pressed into a cylindrical holder capable of holding 6 samples with amounts chosen to give a ruthenium edge step of *ca.* 0.5–1.0. The spectra were obtained at room temperature without treatment and after heating in 4% H_2/He at 150 °C for 1 h and cooled to RT. RuO_2, $Ru(NH_3)_6Cl_3$, $Ru(NH_3)_6Cl_2$, Ru(IV), Ru(III) and Ru(II), respectively, reference compounds were obtained from Aldrich and used to determine the shift in the XANES energy due to change in oxidation state. Phase shifts, backscattering amplitudes were obtained from reference compounds: RuO_2 (4 Ru–O at 1.99 Å and 2 Ru–O at 1.94 Å, or an average of 6 Ru–O at 1.97 Å) and Ru foil (12 Ru–Ru at 2.68 Å). The XANES edge energy was determined from the inflection point of the leading edge, *i.e.*, the maximum in the first derivative. Standard procedures using WINXAS3.1 software were used to extract the EXAFS data. The coordination parameters were obtained by a least square fit in *k*- and *r*-space of the isolated multiple-shell, k^2-weighted Fourier transform data. The samples were also analyzed by X-ray photoelectron spectroscopy (XPS) using a VG Escalab MKII spectrophotometer, which operated with a non monochromatized Mg K source (1253.6 eV).

2.5 Synthesis of Ru–C_{60} nanostructures

In a typical experiment[51] the [Ru(COD)(COT)] (COD = 1,5 cyclooctadiene, COT = 1,3,5-cyclooctatriene) complex was introduced in a Fisher–Porter bottle, and a solution of fullerene C_{60} in the desired solvent was then introduced in the reactor. The resulting purple solution was stirred for 30 min at room temperature, after which the bottle was pressurized with 3 bar of H_2. The solution, which turned black after few minutes of reaction, was kept under stirring overnight at room temperature. After this period of time, excess of H_2 was eliminated and the volume of solvent was reduced under vacuum. Pentane was then added to the colloidal suspension to precipitate the Ru–C_{60} nanostructures. After filtration under argon with a cannula, the black solid powder was washed twice with pentane and filtrated again before drying under vacuum. For each ratio studied, the quantities of reactants are detailed hereafter:

Ru–C_{60} 1/1: 30.0 mg (0.10 mmol) of [Ru(COD)(COT)]; 68.5 mg (0.10 mmol) of fullerene C_{60} and 300 mL of CH_2Cl_2. Yield: 68.1 mg. Ru: 10.6%.

Ru–C_{60} 2/1: 80 mg (0.25 mmol) of [Ru(COD)(COT)]; 91.3 mg (0.126 mmol) of fullerene C_{60} and 400 mL of CH_2Cl_2. Yield: 100 mg. Ru: 16.7%.

Ru–C_{60} 5/1: 200 mg (0.63 mmol) of [Ru(COD)(COT)]; 91.3 mg (0.126 mmol) of fullerene C_{60} and 400 mL of CH_2Cl_2. Yield:129 mg. Ru: 35.6%.

Ru–C_{60} 10/1: 400 mg (1.27 mmol) of [Ru(COD)(COT)]; 91.3 mg (0.126 mmol) of fullerene C_{60} and 400 mL of CH_2Cl_2. Yield: 188 mg. Ru: 48.7%.

Ru–C_{60} 20/1: 100 mg (0.32 mmol) of [Ru(COD)(COT)]; 11.4 mg (0.016 mmol) of fullerene C_{60} and 50 mL of CH_2Cl_2. Yield: 36.9 mg. Ru: 50.4%.

Ru–C_{60} 30/1: 150 mg (0.48 mmol) of [Ru(COD)(COT)]; 11.4 mg (0.016 mmol) of fullerene C_{60} and 50 mL of CH_2Cl_2. Yield: 48 mg. Ru: 54.7%.

Ru–C_{60} 50/1: 250 mg (0.79 mmol) of [Ru(COD)(COT)]; 11.4 mg (0.016 mmol) of fullerene C_{60} and 50 mL of CH_2Cl_2. Yield: 80 mg. Ru: 61.9%.

Growth mechanism. The reaction was performed at −20 °C following the standard procedure: 20 mg (0.064 mmol) of [Ru(COD)(COT)]; 23 mg (0.032 mmol) of fullerene C_{60} and 50 mL of CH_2Cl_2. The reaction was followed by sampling the mixture over the time.

Surface reactivity with CO. The adsorption of carbon monoxide on the surface of the nanostructures was performed in the solid state as follows. A purified sample of nanoparticles was introduced in a Fischer–Porter bottle. The reactor was pressurized with 1.5 bar of CO for 72 h. Then, the CO gas was evacuated under vacuum for 20 min and the ATR-IR spectra were recorded.

3. Results and discussion

3.1 Synthesis and TEM characterization of the Ru–C_{60} nanostructures

Ru–C_{60} nanoarchitectures were synthesized by decomposing [Ru(COD)(COT)] under H_2 (3 bar) in the presence of C_{60} at room temperature. The Ru/C_{60} ratio was fixed to 2/1 and the effect of the solvent the first to be studied. Several solvents (toluene, chlorobenzene, 1,2-dichlorobenzene, dichloromethane, chloroform and decalin) were used under the same reaction conditions except for $CHCl_3$ and CH_2Cl_2, for which higher dilutions were used because of the low solubility of C_{60} in these solvents. TEM analyses of the Ru–C_{60} structures (Fig. 1) show a marked effect of the solvent on the size and shape on the synthesized materials.

The syntheses carried out in decalin lead to structures with very irregular shapes, decorated with small Ru NPs (1.23 ± 0.22 nm). The TEM analyses of the product of the reaction in toluene showed smaller shapeless structures with mean diameters of *ca.* 175 nm. In this case, no NPs were detected from the TEM and HREM analyses (ESI.1†). Spherical particles were systematically obtained using chlorinated solvents or mixtures of toluene and CH_2Cl_2. TEM micrographs of the Ru–C_{60} structures synthesized in chlorobenzene, 1,2-dichlorobenzene, $CHCl_3$, and CH_2Cl_2 reveal spherical particles with mean diameters of 285 ± 3 nm, 200 ± 3 nm, 229 ± 1.5 nm, and 40 ± 0.7 nm, respectively. Ru–C_{60} particles synthesized in CH_2Cl_2 displayed a significantly smaller mean diameter and narrower size distribution; furthermore they were decorated with small Ru NPs (1.15 ± 0.02 nm). STEM-EDX mappings of the structures synthesized in toluene, 1,2-dichlorobenzene and dichloromethane confirm that they are composed of Ru and C even if Ru NPs are not observed (Fig. 2 and ESI.1†).

It is known that polymeric spheres of uniform size can be produced using mechanical methods.[52] In a first step, the polymers form long threads, which break into smaller droplets of uniform size due to Rayleigh instability. The size of the spheres is determined by the applied stress, and weakly depends on the viscosity ratio between the dispersed and the continuous phases.[53,54] The polymer concentration has also an impact on the structure formed.[55] If we assume that the Ru–C_{60} spheres are polymeric and present similar properties (*i.e.* viscosity) in all the synthesis carried out, we can correlate the self-assembly of the polymer in spheres with the solvent viscosity but also permittivity (see ESI.2†). In decalin, which has the higher viscosity and the lower permittivity (see Table 1), no shape control is achieved, while in CH_2Cl_2 (lower viscosity and high permittivity), small spherical particles are produced.

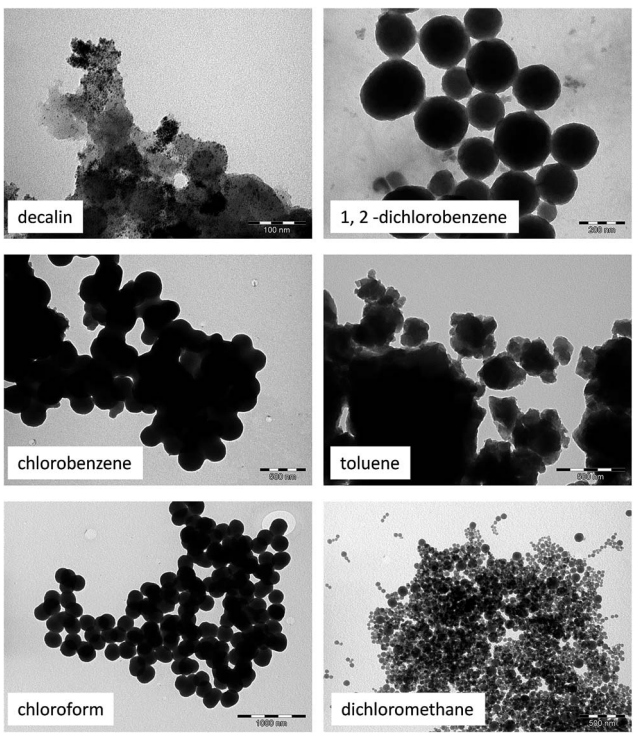

Fig. 1 TEM micrographs of Ru–C_{60} structures with Ru/C_{60} = 2/1 synthesized in different solvents: decalin (scale bar 100 nm), 1,2-dichorobenzene (scale bar 200 nm), chlorobenzene (scale bar 500 nm), toluene (scale bar 500 nm), chloroform (scale bar 1000 nm) and dichloromethane (scale bar 500 nm).

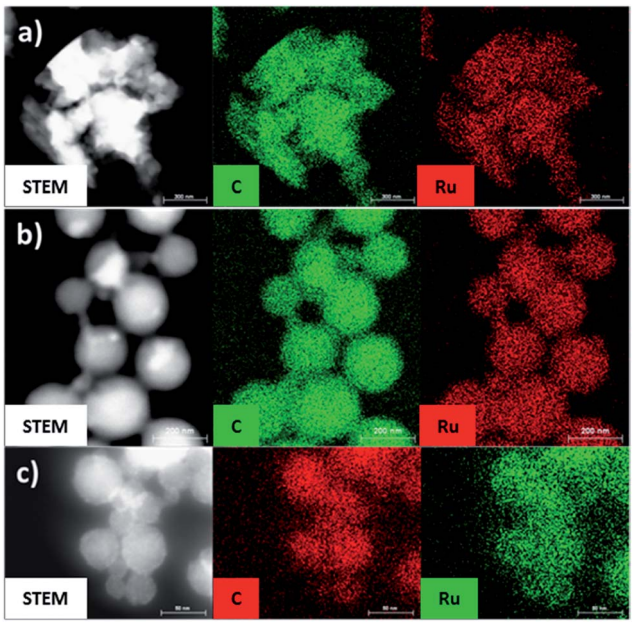

Fig. 2 STEM-EDX mappings of Ru–C_{60} (2/1) structures synthesized in: (a) toluene (scale bar 300 nm); (b) 1,2-dichlorobenzene (scale bar 200 nm); and dichloromethane (scale bar 50 nm).

The other solvents, showing intermediate viscosity, allow obtaining spheres as well, however, with larger mean diameters. The only exception is the material synthesized in toluene, which has, as decalin, a low permittivity. In order to unravel the growth mechanism of the spherical particles we monitored the reaction by *ex situ* TEM analyses. The synthesis was realized in CH_2Cl_2 using a Ru/C_{60} ratio of 2/1 at low temperature (−20 °C) because of the fast formation of the spheres at r.t. TEM micrographs of samples taken at different times are displayed in Fig. 3. As observed for the synthesis of polymeric spheres,[54] in a first step the big droplets deform into long threads: at 5 min of reaction, mainly elongated objects (with sizes ranging from 300 to 1000 nm) are observed together with some spherical particles with diameters *ca.* 130 nm. At 10 min, the size of these objects ranged between 20 and 400 nm.

After 40 min of reaction, big spheres are observed (mean diameter of *ca.* 290 nm), which are clearly formed from the elongated objects. In the synthesis of polymeric particles a second step is observed, where the resulting droplets can again break up into daughter droplets. This second mechanism is much slower. We stirred the reaction overnight and a last sample was observed by TEM after 12 h. This sample shows spherical particles of 37.0 ± 0.3 nm mean diameter and big spherical particles of about 330 nm. These results indicate that a second step towards the formation of smaller spheres is indeed active. TEM images clearly show that the

Table 1 Solvent properties as related to the TEM analyses obtained for the Ru–C_{60} structures

Solvent	Viscosity (mPa s)[56]	C_{60} solubility ([C_{60}], mg mL^{-1})[57]	Relative permittivity (ε_r)[56]	TEM analyses
cis-Decalin	3.042	4.6	2.22	No shape control – structures decorated with Ru NP of 1.23 ± 0.22 nm
trans-Decalin	1.948		2.18	
1,2-Dichlorobenzene	1.324	27	10.12	Spheres of 200 ± 3 nm
Chlorobenzene	0.753	7	5.70	Spheres of 285 ± 3 nm
Toluene	0.560	2.8	2.38	No shape control of the structures of *ca.* 175 nm
Chloroform	0.537	0.16	4.81	Spheres of 229 ± 1.5 nm
Dichloromethane	0.413	0.26	8.93	Spheres of 39.6 ± 0.7 nm decorated with Ru NP 1.15 ± 0.02 nm

small spheres (≈40 nm) are formed from the large 300 nm spheres.

The STEM-EDX maps of the Ru–C_{60} structures synthesized at −20 °C in CH_2Cl_2 (see ESI.3†) confirm that the structures observed in the early stages of the reaction are constituted by Ru and C, as well as the spheres observed at 40 min of reaction. Nagashima *et al.* studied the synthesis of Pd_nC_{60} polymer from [$Pd_2(dba)_3(CHCl_3)$] (dba = dibenzylideneacetone) in toluene

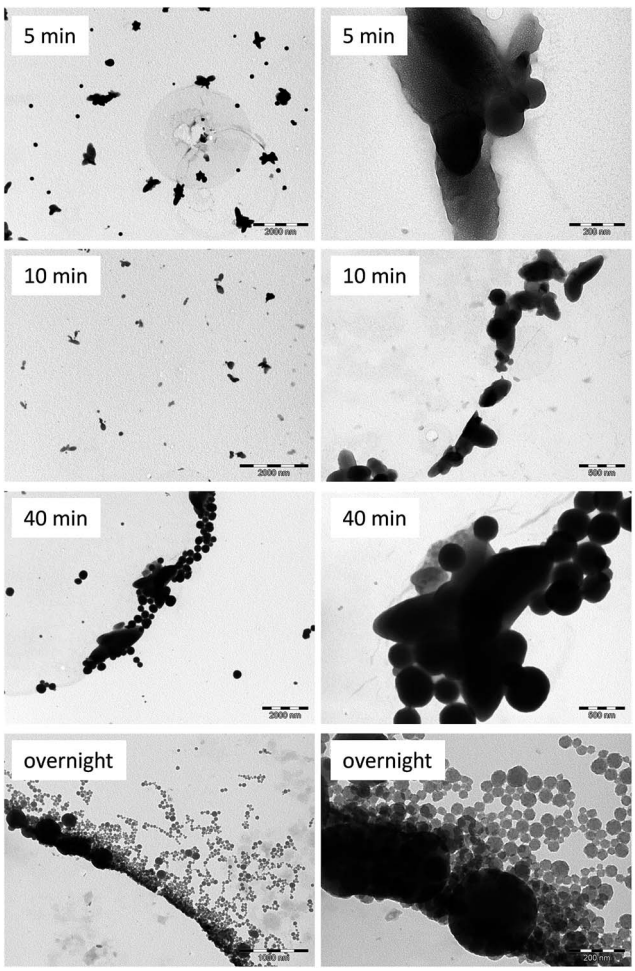

Fig. 3 TEM micrographs of Ru–C_{60} structures synthesized in CH_2Cl_2 using a Ru/C_{60} ratio of 2/1 at −20 °C (scale bar: 5 min, 2000 and 200 nm; 10 min, 2000 and 500 nm; 40 min, 2000 and 500 nm; and overnight, 1000 and 200 nm).

using several Pd/C_{60} ratios.[13] From microprobe analyses, they proposed a mechanism for the formation of $C_{60}Pd_n$, in which a one dimensional polymer $C_{60}Pd_1$ is formed at the first stage. Then, insertion of additional Pd atoms between the polymer chains make bridges to form $C_{60}Pd_n$ ($n > 1$). For $C_{60}Pd_n$ ($n > 3$), an excess of Pd atoms would be deposited on the surface of $C_{60}Pd_3$. In a study on C_{60}–Pd film electrodeposition from palladium acetate, Grądzka *et al.* have shown that in the presence of a large excess of palladium precursor, Pd NPs can be deposited on the polymer surface.[58] In order to better understand the Ru system, we decided to explore the effect of the Ru/C_{60} ratio on the produced Ru–C_{60} structures. Using CH_2Cl_2 as solvent we fixed the concentration of C_{60} and we progressively increased the ruthenium content to obtain Ru/C_{60} ratios of 1, 2, 5, 10, 20, 30 and 50. The TEM images of the synthesized materials are shown in Fig. 4. The TEM and HREM analyses show that the Ru–C_{60} 1/1 sample does not contain Ru NPs. Increasing the Ru content, Ru NPs are observed. Ru NPs display in all cases a small mean diameter, even at high Ru/C_{60} ratios, ranging from 1.10 to 1.35 nm (see Table 2 and ESI.4†). Interestingly, the Ru–C_{60} spheres do not change significantly in size for Ru/C_{60} ratios from 1/1 to 10/1 (≈40 nm, ESI.5†). At a 20/1 ratio, two size distributions are observed for the spheres: the major one centered at 39.8 ± 1.1 nm together with some bigger spheres with mean diameter of 78.8 ± 0.7 nm (see ESI.6 for size histograms†). The Ru–C_{60} 30/1 sample also displayed spheres with a bimodal size distribution (56.4 ± 4.7 nm and 103.2 ± 1.0 nm). At 50/1 ratio the mean diameter of the spheres is 63.3 ± 0.8 nm (Fig. 4 and Table 2). The 30/1, and more particularly, the 50/1 samples are also characterized by the presence of aggregated Ru NPs. These aggregated Ru NPs are very similar to the ones obtained by decomposition of the [Ru(COD)(COT)] precursor in the absence of C_{60} (ESI.7†).

The extremely small size of the Ru species present in the Ru–C_{60} 1/1 sample is a drawback for a classical TEM analysis. To overcome this inconvenient, a scanning TEM in high-angle annular dark field (STEM) approach, based on the Z-contrast dependence, can be useful to identify the small metallic species supported in/on the lighter matrix. For the 1/1 ratio of Ru–C_{60}, the STEM-HAADF micrographs (Fig. 5a and b) show the presence of Ru atoms and/or clusters all over the surface of the spheres. The Ru clusters size does not exceed 0.6 nm. In the case of a representative sphere for the 30/1 ratio (Fig. 5c and d) the HAADF micrographs show the presence of small Ru NPs with

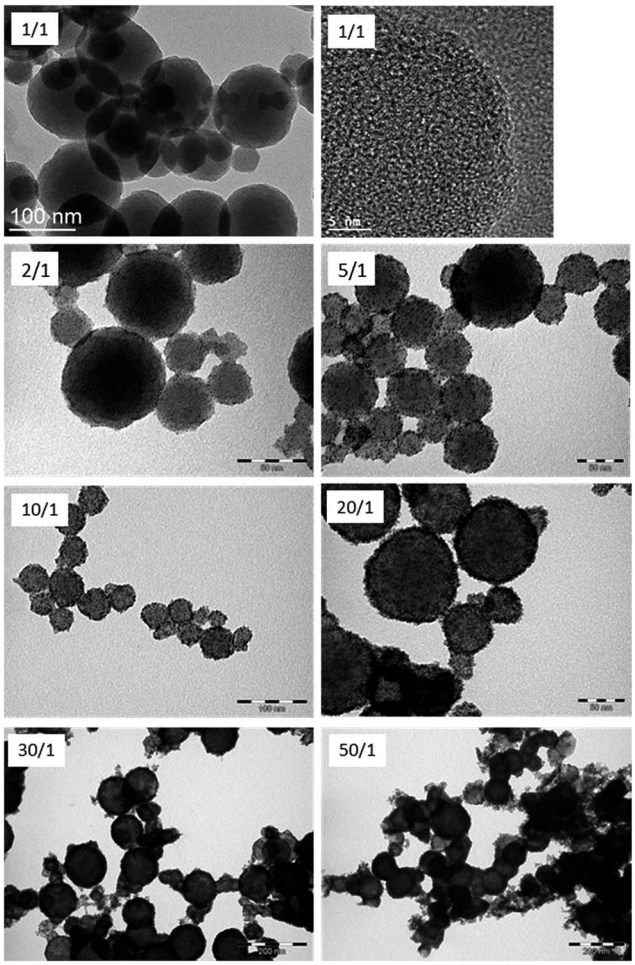

Fig. 4 TEM images of Ru–C_{60} structures synthesized in CH_2Cl_2 using a Ru/C_{60} ratio of 1/1 (scale bar 100 nm and 5 nm), 2/1 (scale bar 50 nm), 5/1 (scale bar 50 nm), 10/1 (scale bar 100 nm), 20/1 (scale bar 50 nm), 30/1 (scale bar 200 nm) and 50/1 (scale bar 200 nm).

a higher concentration of Ru on the surface of the sphere. The distribution of the Ru signal, acquired in STEM-EDX along a line scan, confirms the presence of Ru NPs on the outer sphere surface within the 30/1 sample (ESI.8†), whereas a more

Table 2 Mean size diameters of Ru NPs and spheres of Ru–C_{60} according to the Ru/C_{60} ratio

Ru/C_{60}	Ru (%)	Nanoparticles mean size[a] (nm)	Spheres mean size[a] (nm)
1/1	10.6	Not observed	39.1 ± 0.5 nm
2/1	16.7	1.16 ± 0.02 nm	31.6 ± 0.6 nm
5/1	35.6	1.31 ± 0.03 nm	42.6 ± 1.0 nm
10/1	48.7	1.26 ± 0.03 nm	32.4 ± 0.3 nm
20/1	50.4	1.10 ± 0.01 nm	39.8 ± 1.1 nm|85.2 ± 2.9 nm
30/1	54.7	1.34 ± 0.01 nm	56.4 ± 4.7 nm|103.2 ± 1.0 nm
50/1	61.9	1.35 ± 0.02 nm	63.3 ± 0.8 nm

[a] Manual measurement from enlarged micrographs of at least 200 objects.

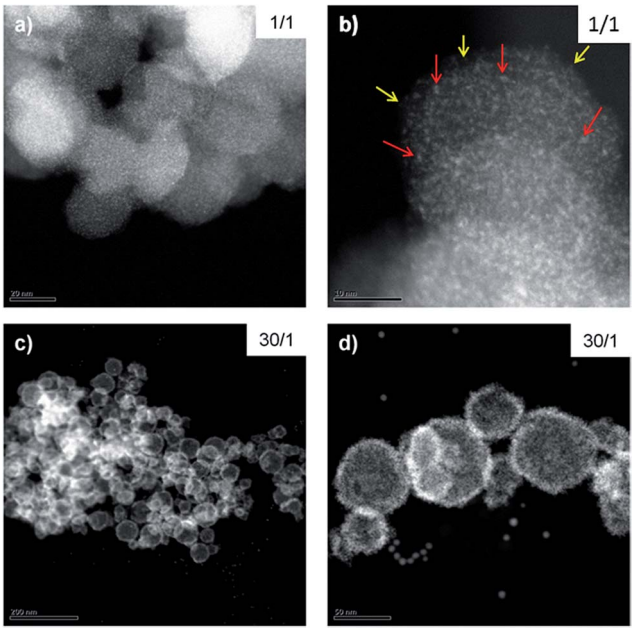

Fig. 5 (a) STEM-HAADF micrographs of Ru/C_{60} 1/1 (scale bar 20 nm), (b) (scale bar 10 nm), (c) STEM-HAADF micrographs of Ru/C_{60} 30/1 (scale bar 200 nm), and (d) (scale bar 50 nm) nanostructures. In (b), the yellow and red arrows point to the Ru few atom clusters and larger clusters, respectively.

uniform distribution of Ru is observed for the 1/1 sample (ESI.8†). The above TEM or STEM analyses on the 2D projections of the objects do not provide clear information on the possible presence of Ru species (clusters or small NPs) in the interior of the spheres. Electron tomography analysis allowed the investigation within the volume of theses spheres.

Fig. 6 shows the results obtained for the 30/1 Ru–C_{60} ratio. From the slices views of 3D reconstructed volumes (Fig. 6b and c), the presence of small Ru NPs is obvious on the surface of the sphere, creating a Ru NP shell with a thickness around 7 nm, which correspond to a multilayered NP structure. This is in agreement with the Ru signal distribution observed in Fig. 5c and d, as the heavier elements appear most contrasted in STEM-HAADF, and also with the distribution of the Ru signal, acquired in STEM-EDX (ESI.8†). It is thus clear that no crystallized Ru NPs are present inside the spheres, but this analysis does not exclude the presence of atomic Ru inside the polymeric matrix. The analysis was also performed for the Ru–C_{60} sample with a 1/1 ratio, but the very small size of the clusters prevents their localization (see ESI.9†), the size of the clusters being below the resolution limit for the electron tomography analysis. The resolution attained in electron tomography is in the nanometer range, thus it is practically impossible to evidence the presence of any metal atoms and/or few-atom clusters within the spheres. It is therefore reasonable to propose that, in CH_2Cl_2, the decomposition of the [Ru(COD)(COT)] precursor leads to the formation of polymeric spheres containing Ru atoms or small clusters and fullerenes at low Ru–C_{60} ratio (≤1), and that further increase of the Ru–C_{60} ratio lead to Ru atoms,

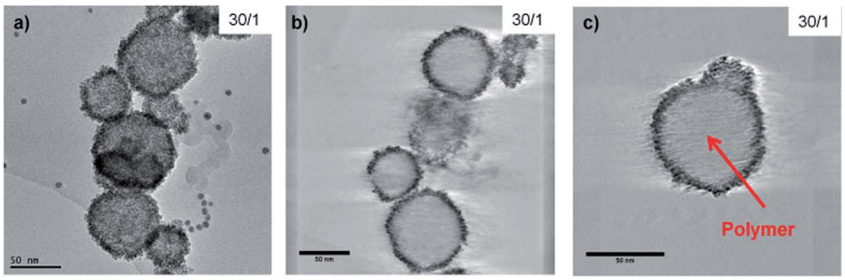

Fig. 6 3D analysis of Ru/C_{60} 30/1 by electron tomography: (a) bright field TEM images at 0° tilt from the tilt series; (b) and (c) representative cross-sectional slices along one direction in the plane of 3D reconstructed volume showing the location of shell of Ru 2 nm size NPs on the surface of the sphere. The thickness of the shell is 7 nm (scale bar 50 nm).

clusters or NPs deposition on the surface of these polymeric spheres.

The addition of extra Ru atoms in the polymeric spheres might be prevent by diffusional limitations. We checked independently that the decomposition of an excess of [Ru(COD)(COT)] on the Ru–C_{60} 1/1 sample, to reach a 10/1 ratio, leads to NPs deposition outside the Ru–C_{60} 1/1 spheres (ESI.10†).

Cold FEG confirmed de absence of clusters on the Ru–C_{60} matrix of 1/1 sample (Fig. 7).

3.2 DFT calculations on the Ru–C_{60} nanoarchitectures

There are five possible sites on C_{60} surface where Ru atoms may be adsorbed: (i) an atop site (η^1) on which the Ru atom is coordinated to a single carbon atom, (ii) a bridge site between two hexagonal rings ($\eta^{2(6)}$), (iii) a bridge site between pentagonal and hexagonal rings ($\eta^{2(5)}$) on which a Ru atom sits on the C–C bond and forms two Ru–C bonds, (iv) a hollow site above the center of a pentagonal ring of C atoms (η^5), and (v) a hollow site above the center of a hexagonal ring of C atoms (η^6).[59] For a single Ru atom interacting with one C_{60}, the most stable configuration is $\eta^{2(6)}$, with an adsorption energy of −48 kcal mol^{-1}, followed by $\eta^{2(5)}$, η^6, η^5, with energies of −39, −38, and −35 kcal mol^{-1} respectively, when the atop site is instable. The better stability of the $\eta^{2(6)}$ site is not surprising, as the double bond shared by two hexagons corresponds to a maximum of the electronic density of the fullerene. Experimentally, this coordination mode has been observed for Pt complexes and suspected for Ru ones.[60] These adsorption energies are significantly larger than the ones obtained for Ni, Au or Ta atoms for instance, with typical values smaller than −25 kcal mol^{-1},[31,33,34] but remain in very good agreement with values obtained for Rh, Ir, Pd and Pt atoms.[36] Pt atoms bind more strongly than Ru ones on C_{60} since, using the same computational settings; the adsorption energy of a Pt atom is already −66 kcal mol^{-1}. This value is also in good agreement with previously reported values.[36,61,62] For the $\eta^{2(6)}$ and $\eta^{2(5)}$ sites, the smallest Ru–C bond lengths are 2.06 Å. Then, the Ru–C bond length increases with the increase of adsorption energy for the different sites. For the η^6 site, two Ru–C bond-lengths are 2.25, two others Ru–C distances are 2.34 when the last ones are 2.42 Å. It means that a single Ru prefers to lie in a displaced hollow site than a highly symmetric site. Finally, the Ru–C distances in the less stable site, *i.e.* in the η^5 position, are 2.21 Å. Interestingly the most stable Ru–C_{60} complex is magnetic with a moment of 2 μ_B.

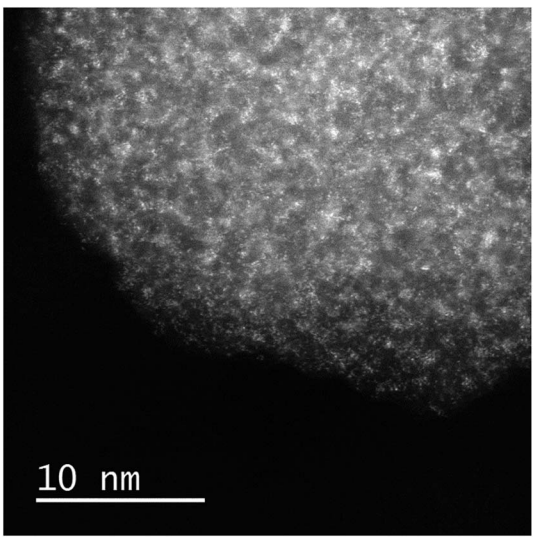

Fig. 7 STEM-HAADF micrographs of Ru/C_{60} 1/1.

If now, we take into account the real source of Ru in the calculation, the [Ru(COD)(COT)] precursor, we have to consider that it may coordinate even when it is partially decomposed. The [Ru(COD)] species adsorbs, in a $\eta^{2(6)}$ site, with two short Ru–C bond-lengths of 2.11 Å and adsorption energy of −58 kcal mol^{-1}. The η^1 site has almost the same energy but with a smaller Ru–C distance, *i.e.* 2.04 Å. On the contrary, the [Ru(COT)] species has a preference for the η^1 site, with an adsorption energy of −38 kcal mol^{-1}, the $\eta^{2(6)}$ site is 4 kcal mol^{-1} higher. However when using the following energy balances: [Ru(COD)(COT)] + C_{60} → [Ru(COT)]@C_{60} + COD or [Ru(COD)(COT)] + C_{60} → [Ru(COD)]@C_{60} + COT, meaning that we take into account the precursor dissociation energy, the energy differences become largely positive: +21 and +28 kcal mol^{-1}, respectively. As a result the precursor has to be completely decomposed by the action of H_2 in order to allow for the creation of Ru–C_{60} bond, and no partially decomposed Ru complexes can be stabilized on C_{60} surfaces.

In interaction with 2 fullerenes, a single Ru atom will preferably coordinate in a η^2–η^2 position, bridging two $\eta^{2(6)}$ positions, with 4 Ru–C bond-lengths of 2.07 Å, as shown in Fig. 8a.

This complex adopts then a dumbbell like structure, as for a Ni[31,63] or Pt atoms.[36,61,62] The corresponding stabilization energy of this nonmagnetic complex is large, −44 kcal mol^{-1}, when adding a C_{60} to an existing Ru–C_{60} complex. However, this binding energy for a Ru complex is still lower than the value of −65 kcal mol^{-1}, obtained at a semi-empirical level, on a C_{60}–Pt–C_{60} complex.[62] It suggests again that a Ru atom has a little less affinity for C_{60} than a Pt one. Interestingly, another stable structure that exhibits a $\eta^{2(6)}$–η^6 coordination mode, as it can be seen from Fig. 8b, lies only 12 kcal mol^{-1} higher in energy. The corresponding Ru–C distances are ranging from 2.07 to 2.85 Å for this site that connects 8C to the Ru atom. This relatively small energy difference between the two coordination modes can be reduced by 5 extra kcal mol^{-1} due to the presence of adsorbed hydrogen atoms on the C_{60}, as proposed experimentally, *cf.* Section 2.3, in the vicinity of the Ru atom (ESI.11†). Indeed a significant change of the Ru coordination is observed upon H_2 adsorption since the most stable structure possesses a $\eta^{2(6)}$–η^4 character. More details on the H_2 adsorption thermodynamics are provided in ESI.† In the case of the dumbbell like structure (Fig. 8a) it seems obvious that a third C_{60} can be easily coordinated to the central Ru atom. This reaction is still thermodynamically favorable but the energy gain is only −11 kcal mol^{-1}, due to the coordination mode of the third fullerene that is η^1. This stable $Ru(C_{60})_3$ configuration might be viewed as a potential linker between ideal linear polymeric chains, as described in the following. The two C_{60}–Ru–C_{60} complexes (Fig. 8a and b) can thus be viewed as elementary bricks for hypothetical 1D chains made of –C_{60}–Ru–C_{60}– with a 1Ru/1C_{60} ratio. Fig. 8d shows a first model made of a unit cell that contains only 1Ru and 1C_{60}. The corresponding optimized lattice constant is around 10.4 Å. In this particular state, the four smallest Ru–C distances are lying in 2.04 to 2.11 Å range and two others are at 2.42 and 2.45 Å, when the next nearest C atoms are 2.66 Å away. As a consequence the Ru atom has a $\eta^{2(6)}$–η^4 coordination mode in this case. To allow for more flexibility in the coordination mode, we have also used a model made of 2Ru atoms and 2C_{60} in the calculation cell. As a result of rotating slightly one of the C_{60} molecule on a vertical axe, a $\eta^{2(6)}$–η^6 coordination mode is stabilized, as shown in Fig. 8e.

In this structure a Ru atom does not have a perfect hollow position with 8 different Ru–C bond-lengths: 2.04, 2.11, 2.14, 2.18, 2.34, 2.44, 2.53 and 2.57 Å. Almost the same values are yielded for the second metallic center (Fig. 9). This coordination mode is in good agreement with EXAFS results as shown below.

If we now try to complete the coordination sphere of one Ru atom by approaching a H_2 molecule, it spontaneously dissociates and push the Ru to change its coordination to be $\eta^{2(6)}$–η^3 with two additional Ru–H distances are 1.59 Å, see Fig. 8f. When these two hydrides are transferred to one of the C_{60}, the $\eta^{2(6)}$–η^6 coordination modes are recovered but with a slight elongation of the largest Ru–C distances, that are now between 2.60 and 2.70 Å (Fig. 8g). In these cases, the Ru atoms provide large electronic density to the neighboring C_{60}, with a charge transfer of around 0.6e^-. This value is not surprising since C_{60} is a well-known electron acceptor and it is in reasonable agreement with Raman spectroscopy results, see below.

From the different microscopy techniques, it seems obvious that outside the spheres that contain the polymeric phase, Ru NPs are formed. To propose an answer at the molecular level of this statement, we have addressed two issues: are the thermodynamics in favor of Ru NPs formation? Could it be the solvent that protects metallic atoms and avoid Ru–Ru formation bonds?

Starting from an ideal polymeric 1D chain, and thus adding a second metal atom is indeed energetically favorable; as well as adding 2 other ones, as it can be seen in Table 3. An interesting feature is that the lattice parameter values are increased to accommodate the creation of new Ru–C bonds, and thus could be experimentally detected. Moreover the distance between the two Ru_1–Ru_2 in Fig. 10a is very unusual for metallic bond with a value of 2.28 Å. With 4Ru atoms, see Fig. 10b, the Ru_4–Ru_2 bond-length is 2.26 Å, the Ru_1–Ru_2 is slightly elongated (+0.09 Å) when the last one is 2.35 Å. From Table 3, where energy gains per Ru atom are compiled in various binding situations, *i.e.* in single complex with different ratio Ru/C_{60}, in some ideal 1D polymeric chains or even in small cluster models and finally in the bulk, we can provide some interesting insights of the reaction media behavior. Indeed, when comparing the stabilization energies of a Ru atom involved in a 1D chain, and one in small

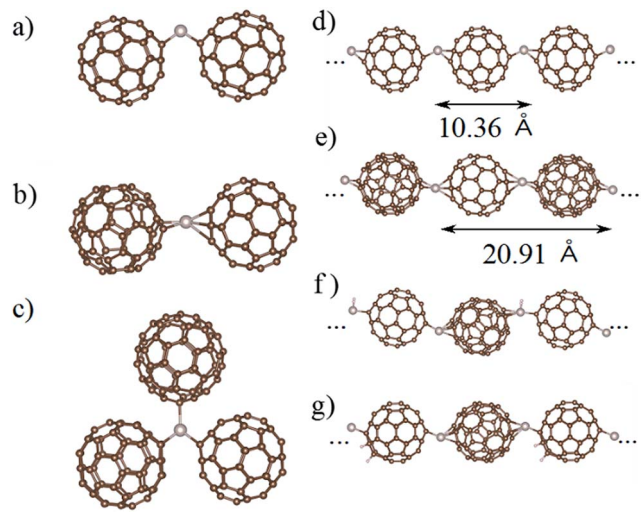

Fig. 8 (a) Side views of C_{60}–Ru–C_{60} complex in the dumbbell like structure, (b) in the $\eta^{2(6)}$–η^6 coordination mode, and (c) of the most stable Ru–$(C_{60})_3$ complex. (d) Ideal 1D chains and their corresponding lattice parameters for 1Ru/1C_{60} ratio for the $\eta^{2(6)}$–η^4 in state, and (e) for the $\eta^{2(6)}$–η^6 state. (f) Partially hydrogenated ideal polymeric chains with one Ru atom hydrogenated, and (g) with one C_{60} hydrogenated. Ru atoms are in grey, carbon atoms in brown and H in white.

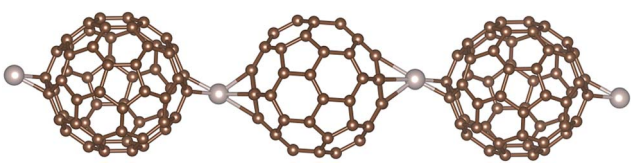

Fig. 9 Side view of an ideal 1D chain for 1Ru/1C_{60} ratio in the $\eta^{2(6)}$–η^6 state. Ru atoms are in grey, carbon atoms in brown.

Table 3 Energy stabilization per Ru atom in various systems: for single C_{60}–Ru complexes, for different linear chains with different Ru/C_{60} ratio, for two pure small metallic nanoparticles and in the bulk, with isolated Ru atom serving as the energy reference

Systems	Energy gain (kcal mol^{-1})
C_{60}–Ru	−48
$(C_{60})_2$–Ru	−92
$(C_{60})_3$–Ru	−103
…–C_{60}–Ru–C_{60}–…	−86
…–C_{60}–Ru_2–C_{60}–…	−94
…–C_{60}–Ru_3–C_{60}–…	−106
…–C_{60}–Ru_4–C_{60}–…	−76
Ru_{13}	−96
Ru_{55}	−123
Ru bulk	−153

clusters or even worse in the bulk, it is clear that a Ru atom prefers to bind to other Ru atoms.

If one considers Ru_{13} cluster formation energy (−96 kcal mol^{-1}) the two processes are thermodynamically favorable. At this step, one can assume that the polymeric phase, with a ratio close to 1Ru/1C_{60} without excluding small clusters of Ru_n ($n \leq 3$) linking fullerenes is the kinetic product of the reaction and then larger Ru NPs are created, producing the thermodynamic products of the reaction. To support this idea we have also calculated the binding energy of Ru_{13}–$(C_{60})_x$ complexes with x up to 6. The corresponding values are slightly lower than the other values given in Table 3: the energy gain per C_{60} is maximal for $x = 1$ and $x = 2$, with −87 and −88 kcal mol^{-1} respectively, and decreases when x increases: −77, −74, −61 kcal mol^{-1}. See ESI.12† for molecular models of the stable Ru_{13}–C_{60}, Ru_{13}–$(C_{60})_2$, and Ru_{13}–$(C_{60})_6$ complexes. It means that when fullerenes are in excess, they have also the possibility to strongly bind metallic NPs.

However, in the present theoretical picture of the system, it is not clear why the polymeric phase is stabilized and has a net preference for the 1Ru/1C_{60} ratio. To propose a reasonable explanation, at the atomic scale, we have further investigated the effects of two different solvent molecules, *i.e.* toluene and dichloromethane, on the stabilization of the polymeric phase. Since the solvent molecules interact only weakly with the metallic center, see ESI.13† for a more detailed discussion, the main reason is only a steric effect that avoid the agglomeration of Ru atoms.

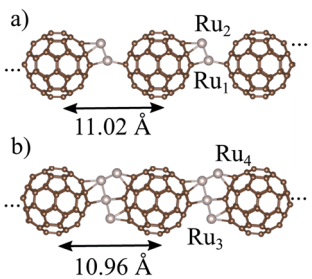

Fig. 10 (a) Side views and lattice parameters corresponding to a 2 Ru/C_{60} and (b) 4 Ru/C_{60} ratio. Ru atoms are in grey, carbon atoms in brown.

3.3 Infrared, NMR and Raman characterization

The attenuated total reflectance infrared (ATR-IR) spectra were recorded for Ru–C_{60} samples in the solid state (ESI.12†). Characteristic peaks of C_{60} are observed at 524, 576, 1182 and 1422 cm^{-1}, together with other vibrations in the ranges 2800–3000 cm^{-1} (C–H stretching) and 400–1600 cm^{-1} (C–H bending, C–C stretching, C–H out of plane). Some of the peaks have been attributed to $C_{60}H_{18}$ (ref. 64) and $C_{60}H_{36}$ (ref. 65) species, the rest of the peaks are probably due to the presence of a mixture of hydrofullerenes with different number of hydrogen atoms.[66,67] The presence of fullerene in the samples was also confirmed by MAS $^{13}C\{^1H\}$ NMR, with a signal at 143.2 ppm for Ru–C_{60} 1/1, 2/1, 5/1 and 10/1 samples (see ESI.13†). The $^{13}C\{^1H\}$ MAS NMR also show a low intensity broad signal at 40 ppm. The CP-MAS ^{13}C NMR (CP = ^1H–^{13}C cross polarization) allowed to clearly observe the broad signal at 40 ppm, which increased the intensity with increasing the Ru content. We attributed this broad signal to the presence of a mixture of hydrogenated fullerenes,[64,68–72] as observed by ATR-IR. This was also confirmed by ^1H MAS NMR with the presence of a large peak at 4.5 ppm. However, the low intensity of these peaks indicates that fullerene hydrogenation is only a side reaction. If usually high temperatures and pressures are necessary for fullerene hydrogenation,[73,74] the hydrogenation of C_{60} on Rh/Al_2O_3 catalyst at ambient temperature and pressure has already been reported.[75]

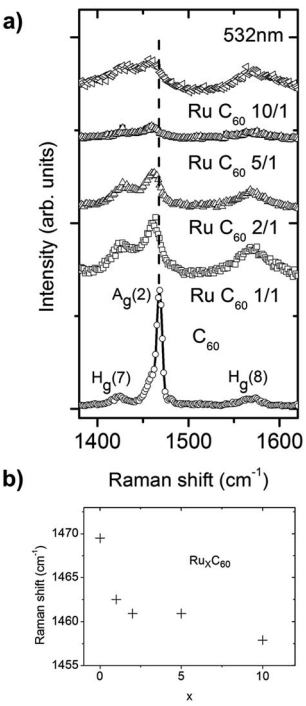

Fig. 11 (a) Raman spectra excited at 532 nm of C_{60} and Ru–C_{60} 1/1, 2/1, 5/1 and 10/1 samples in the spectral range of the tangential pitch mode $A_g(2)$; and (b) Raman spectral position of the $A_g(2)$ band as a function of molar concentration of C_{60}.

Since carbon monoxide is a sensitive probe for studying the surface composition of metal NPs, the CO adsorption on the Ru–C_{60} nanostructures was investigated by ATR-IR. Carbon monoxide was reacted with solid samples of Ru–C_{60} in a Fisher–Porter bottle under mild conditions (1.5 bar of CO, r.t., 24 h). Then, ATR-IR spectra were recorded with a spectrometer available in a glove box (ESI.12b†). After CO exposure Ru–C_{60} 1/1, 2/1, 5/1 and 10/1 samples display three new peaks between 1900 and 2130 cm^{-1}, which are typical of adsorbed terminal CO species. In the Ru–C_{60} 1/1 nanostructure, the peaks appear at 1998, 2053 and 2120 cm^{-1}. The $[Ru(CO)_3(alkene)_2]$ complexes typically show three adsorption bands in the CO stretching region, in particular $[Ru(CO)_3(C_2H_4)_2]$ complex display three bands at 2081, 2005 and 1995 cm^{-1}.[76–78] Considering that C_{60} acts as an electron-deficient olefin, the bands should be shifted to highest stretching frequencies in a $[Ru(CO)_3(\eta^2\text{–}C_{60})_2]$ species compared to $[Ru(CO)_3(C_2H_4)_2]$, fitting with the spectrum obtained for the Ru–C_{60} 1/1 nanostructure, *i.e.* CO molecules are likely to coordinate to the Ru atoms in a polymeric structure to form species such as $[Ru(CO)_3(\mu\text{-}\eta^2,\eta^2\text{-}C_{60})]_\infty$. However, species containing more or less CO ligands, as well as a mixture of species, cannot be discarded, as the signals are relatively broad. Ru–C_{60} 2/1, 5/1 and 10/1 samples show the same pattern, although the signal at 1998 cm^{-1} becomes broader when increasing the Ru content. We assigned this broad signal, which increases in intensity with the number of Ru NPs present on the sample, to terminal CO adsorbed on the Ru NPs surface as it usually appears in the region of 1970–2000 cm^{-1}.[79,80] For higher Ru–C_{60} ratios, the ATR-IR signal intensity was too low for interpretation.

C_{60} is a well-known electron acceptor and Raman spectroscopy can give valuable information on charge transfer. Fig. 11a shows Raman spectra excited at 532 nm of C_{60} and Ru–C_{60} 1/1, 2/1, 5/1 and 10/1 samples, in the spectral range of the tangential pitch mode $A_g(2)$. It has been shown that the energy of the $A_g(2)$ mode (1468 cm^{-1} for pure C_{60}) is sensitive to charge transfer when evaporating C_{60} on metal surfaces,[81] or for transition metal fullerides.[19] While the charge transfer depends on the work function of the metal, other factors such as screened metal–adsorbate interactions and the effect of covalent bond

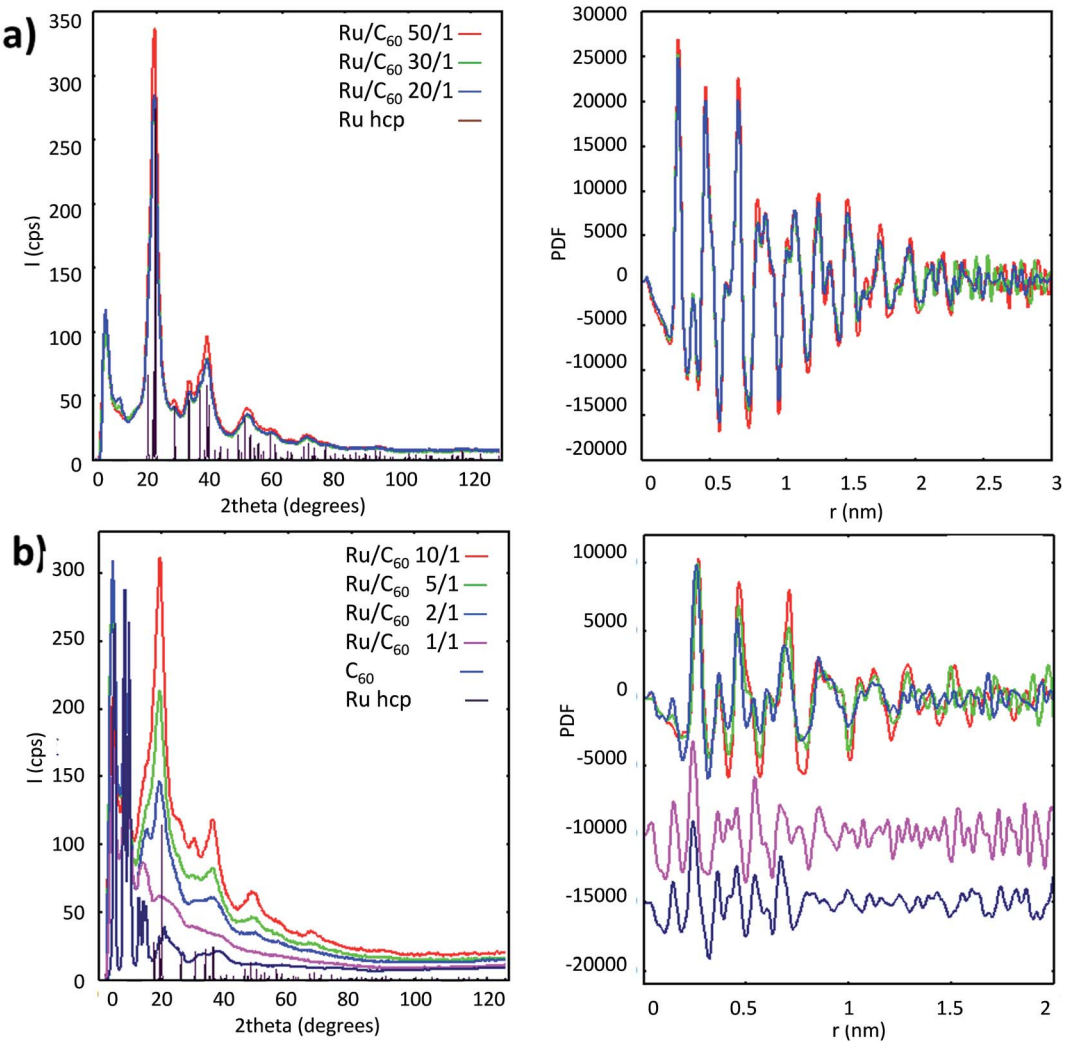

Fig. 12 (a) Left – diffractograms for high Ru/C_{60} ratio together with Ru hcp reference data, right – related PDF. (b) Left – diffractograms for lower Ru/C_{60} ratio with Ru hcp reference data, right – related PDF.

formation may also influence the observed spectral shift, but are believed to be less important. It is commonly accepted that this mode is downshifted by approximately 6 cm^{-1} transferred to C_{60} in ionic fulleride compounds. For C_{60} alkali metals the downshift is directly proportional to the number of metal atoms since each atom donates one electron. The relationship between shift and composition is more complicated for the transition metal fullerides since these compounds may exhibit a large proportion of covalent bonding between metal and C_{60}. The $A_g(2)$ mode downshift observed for Pd–C_{60} and Pt–C_{60} fullerides is 15 cm^{-1}, and it suggests that these fullerides have a structure with the metal atoms connected by a η^2-bonding to two neighboring C_{60} molecules. From the work function of Ru (4.71 eV) one would expect a similar spectral shift as for Cu (4.70 eV) of −23 cm^{-1}. We observe here a spectral shift as large as −10.1 cm^{-1} for the Ru–C_{60} 10/1 sample, and a significant broadening with increasing amount of C_{60} caused by strong electron–phonon interaction. For the Ru–C_{60} 1/1 sample, the spectral shift is of −6 cm^{-1}. The spectrum of C_{60} without Ru is shown at the bottom of Fig. 11a for comparison. The fact that the spectra with Ru do not show a superimposed spectrum of C_{60}, demonstrates that the C_{60} is strongly interacting with Ru. The $A_g(2)$ mode downshift difference between the Ru–C_{60} and Pd–C_{60} and Pt–C_{60} fullerides might be due to a different coordination mode: a η^2-bonding to two neighboring C_{60} for Pd–C_{60} and Pt–C_{60}, and η^2 and η^6 for the Ru–C_{60} fulleride. The charge transfer to the C_{60} molecules is therefore not only dependent on the metal but also on the type of covalent bonds. The charge transfer was also evidenced by XPS, by comparing the binding energy of Ru3p3/2 (462.2 eV) with that of metallic ruthenium (461.2 eV). Fig. 11b shows how the spectral shift progressively saturates at higher molar concentration of C_{60}. No sizeable spectral shifts are observed for the $H_g(7)$ and $H_g(8)$ modes, which is consistent with only smaller shifts observed for C_{60} on Cu (<7 cm^{-1}). The smaller observed spectral shift observed for the Ru–C_{60} samples compared to metal surfaces, indicates that the work function of the Ru species is larger than for bulk Ru.

3.4 WAXS and EXAFS characterization

Samples sealed in Lindemann glass capillaries were measured by WAXS using a diffractometer dedicated to pair-distribution function (PDF) studies (low background, Mo radiation). For the samples with high Ru/C_{60} ratio, the obtained diffractograms are very close and fully consistent with metallic Ru in the hcp system (Fig. 12a) with no significant contribution of C_{60}. After corrections and Fourier transforms, the related PDF functions are as expected also very close, and consistent with metallic Ru NPs with low structural disorder and sizes (from coherence length) reaching 2.5 nm. From the shape of the envelope characterized by a rapid initial decrease and a secondary maximum for a larger value (*ca.* 1.5 nm) before the final decrease, size dispersion is likely, with a large proportion of NPs much smaller than the 2.5 nm value. This is in agreement with TEM measurements. Evolution is much different for smaller Ru/C_{60} ratios: for 10/1, 5/1 and 2/1, we first observe (Fig. 12b) a gradual decrease of the peaks characteristic of the Ru hcp structure, then for the 1/1 ratio the hcp crystalline signature totally vanishes and the diffractogram is closer to the one obtained for pure C_{60}, excepted for the sharp peaks at low angle observed only for the highly ordered pure C_{60} sample. The main

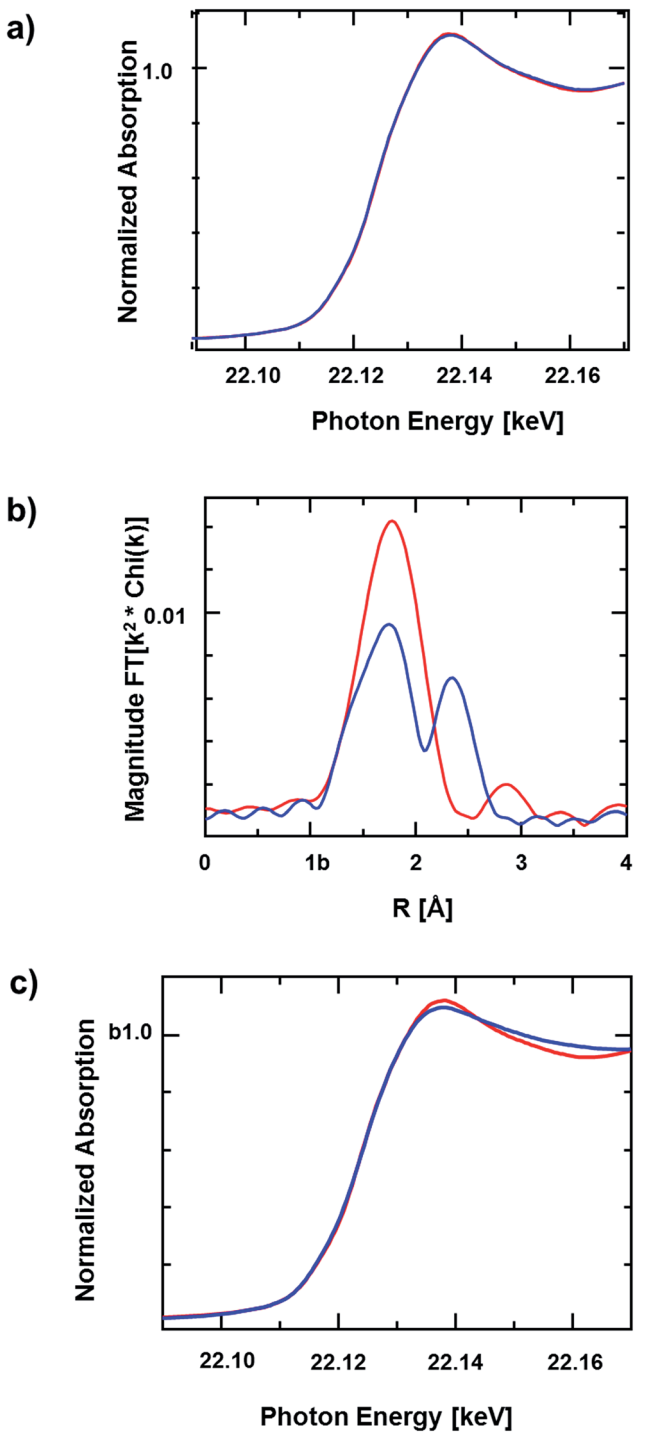

Fig. 13 (a) Ru K-edge XANES from 22.09 to 22.17 keV (red: Ru–C_{60} 1/1 N_2 at RT, and blue: Ru–C_{60} 1/1H_2 at 150 °C); (b) magnitude of the Fourier transform of k^2-weighted Ru EXAFS (k^2: Δk = 2.8–11.3 $Å^{-1}$) (blue: Ru–C_{60} 2/1, H_2 at 150 °C, red: Ru–C_{60} 1/1, H_2 at 150 °C); and (c) Ru K-edge XANES from 22.09 to 22.17 keV (blue: Ru–C_{60} 1/1, H_2 at 150 °C red: Ru–C_{60} 2/1, H_2 at 150 °C).

Table 4 Ruthenium EXAFS fits of samples Ru–C_{60} 1/1 and 2/1

Sample	XANES energy, keV	Scatter	N	R, Å	$\Delta\sigma^2$ ($\times 10^3$)	E_o, eV
Ru foil, ref	22.1170	Ru–Ru	12	2.68	0.0	8.5
RuO_2	22.1285	Ru–O	5.8	1.97	3.0	0.5
$Ru(NH_3)_6Cl_3$	22.1268					
$Ru(NH_3)_6Cl_2$	22.1248					
Ru–C_{60} 1/1, N_2 at RT	22.1244	Ru–C	8.3	2.21	3.0	7.7
Ru–C_{60} 1/1, H_2 at 150 °C	22.1244	Ru–C	8.3	2.21	3.0	8.7
Ru–C_{60} 2/1, H_2 at 150 °C	22.1241	Ru–C	5.1	2.21	3.0	9.4
		Ru–Ru	2.2	2.63	4.0	1.5

interest of PDF analysis is the capability to go beyond crystalline order and to analyze characteristic distances in the material, related to crystalline periodicity or not. In the present case, we observe on the PDF a decrease of the metallic Ru order, however mostly marked for the longer distances for the 10/1, 5/1 and 2/1 ratios, actually indicating Ru NPs with a more single size distribution and an average diameter close to 1.5 nm for the 2/1 ratio. For the 1/1 ratio (ESI.14†), we observe a drastic change for the distances in the 0.2–0.3 nm range: for 2/1, we can still observe the Ru–Ru bonding distance (0.265 nm in bulk Ru), it however fully vanishes for 1/1, which in this range of distances is indeed very close to pure C_{60}. Distribution of distances in this range may also quite well accommodate bonds between Ru atoms and light elements, especially C (the 0.21–0.23 nm range for the Ru–C bonding distance is quite common).

In addition, *ab initio* calculations, as well as the results of our DFT calculations, show a significant contraction of the bond lengths for Ru_n clusters (n < 13): Ru–Ru bonding distance between 0.21 and 0.24 nm. However, since non-bonding C–C distances from C_{60} obviously also pile up there, such agreement with PDF is however not a clear evidence of Ru–C or Ru–Ru bonds. All these elements clearly indicate that for the 1/1 ratio, there is no evidence of Ru NPs, although we cannot completely discarded some metallic bonding for Ru atoms in small clusters in this sample. Order is dominated by the C_{60} structure for short distances, but discrepancies for distances above 0.7 nm strongly indicate more extended ordering, however difficult to safely characterize. Short distances are also in good agreement with eventual Ru–C bonding. For the 2/1 ratio, small Ru NPs (*ca.* 1.5 nm) can be observed. For the 5/1 ratio and above, these small NPs can still be observed but associated to an increasing proportion of larger NPs (2.5 nm from coherence length), which suggests increasing coalescence from small NPs.

EXAFS analyses. The Ru K-edge X-ray absorption spectra of samples Ru–C_{60} 1/1 and 2/1 were obtained in N_2 (as synthesized) and after heating in 4% H_2/He for 1 h at 150 °C. The X-ray absorption near edge (XANES) spectra of Ru–C_{60} 1/1 in N_2 and after high temperature treatment are shown in Fig. 13a. The XANES energy is 22.1244 keV for both spectra and the shape of the XANES does not change after hydrogen treatment indicating no change in the Ru oxidation state, or structure after high temperature treatment under H_2. The magnitude of the Fourier transform of Ru–C_{60} 1/1 after high temperature H_2 (Fig. 13b) shows a peak below about 2 Å (phase uncorrected distance) and a small peak at longer distance. The fit of the Fourier transform is given in Table 4. The low R peak is fit with a Ru–C phase and amplitude functions calculated by FEFF, and gives 8.3 Ru–X bonds at 2.24 Å. Typical Ru–O bonds are below 2.0 Å, while Ru–C are longer at about 2.2 Å, thus it is likely that the light scatter is Ru–C. Within the error of the analysis the fits of the sample treated in H_2 at 150 °C is identical to that in N_2 at r.t. In both the N_2 and H_2 spectra there is no indication of Ru–Ru scatters typical of metallic Ru NPs. There is a small peak at about 3 Å, which is likely due to a Ru–C–Ru scatter; however, the peak is too small to fit reliably. The XANES and magnitude of the Fourier transform of Ru–C_{60} 1/1 and 2/1 heated to 150 °C in H_2 are shown in Fig. 12c and b, respectively.

The XANES energy of Ru–C_{60} 2/1 is the same as Ru–C_{60} 1/1, *e.g.*, 22.1244 keV; however, the shape of the XANES is slightly different, indicating some small difference in structure. The magnitude of the FT of Ru–C_{60} 2/1 shows that there are fewer light scatters and a new higher R peak at about 2.5 Å (phase uncorrected distance). Fits of the EXAFS spectra indicate there are fewer Ru–C, 5.1 Ru–C at 2.24 Å, compared to sample Ru–C_{60} 1/1. In addition, the scatter at longer R is due to Ru–Ru scatter with a coordination number of 2.2 at 2.63 Å, typical of metallic Ru NPs. Since non-metallic Ru–C has 8 bonds, a coordination number of 5.1 indicates that approximately 61% of the Ru is bonded to C in the Ru–C_{60} 2/1 sample. The remaining Ru is, therefore, metallic, *i.e.*, 39%. For the metallic fraction the true coordination number is the measured coordination number divided by the fraction of metallic Ru, or 2.2/0.39, or 5.6. For fcc and hcp metals a coordination number of 5.6 is consistent with a particle size of about 1.5 nm.[82] In summary, sample Ru–C_{60} 1/1 has 8 Ru–C bonds, which are stable to reduction in H_2 at 150 °C; while in sample Ru–C_{60} 2/1 approximately one-third of the Ru is reduced to 1.5 nm metallic Ru NPs. In the latter, the remaining two-thirds Ru–C are identical to those in Ru–C_{60} 1/1 sample.

4. Conclusions

In summary, the decomposition reaction of [Ru(COD)(COT)] in the presence of C_{60} has been investigated, and the product(s) of the reaction characterized. The choice of the solvent affects the course of the reaction. Spherical particles are selectively produced in solvent with low viscosity and high permittivity, such as dichloromethane. The particle size depends on the nature of the solvent. According to the Ru/C_{60} ratio, these

spherical particles can be surface decorated with metallic Ru NPs (1.5–2.5 nm), which are stabilized by C_{60}. The structure of the spherical particles has been studied. TEM, EXAFS, WAXS, and DFT calculations point to a polymeric structure, in which each Ru atoms is coordinated to two C_{60}, with a $\eta^{2(6)}$–η^6 coordination mode. Solvent molecules contribute to stabilize this fulleride. This polymeric phase is the kinetic product of the reaction. Then, larger Ru NPs are created on their surface, producing the thermodynamic products of the reaction. During the decomposition reaction under hydrogen, partial hydrogenation of the fullerene occurs, catalysed by the ruthenium. Significant charge transfer from ruthenium to fullerene has been evidenced by Raman spectrometry and XPS for all the prepared materials, which is an important factor to take into account, particularly if we consider the possible reactivity of this fulleride. We believe that these results should open the possibility to draw structure/properties relationships.

Acknowledgements

This work was supported by the Centre National de la Recherche Scientifique (CNRS), which we gratefully acknowledge. The authors acknowledge financial support from the program of China Scholarships Council (CSC) for F. L. grant. I. C. Gerber also acknowledges the Calcul en Midi-Pyrénées initiative-CALMIP (Project p0812) for allocations of computer time. Part of this work was also performed using HPC resources from GENCI-IDRIS and CINES (Project x2015096649).

References

1 F. Giacalone, N. Martín and F. Wudl, in *Fullerene Polymers*, Wiley-VCH Verlag GmbH & Co. KGaA, 2009, pp. 1–14.
2 B. Coq, J. Marc Planeix and V. Brotons, *Appl. Catal., A*, 1998, **173**, 175–183.
3 N. F. Goldshleger, *Fullerene Sci. Technol.*, 2001, **9**, 255–280.
4 B. Machado and P. Serp, in *Nanostructured Carbon Materials for Catalysis*, The Royal Society of Chemistry, 2015, pp. 312–411.
5 R. Loutfy and S. Katagiri, in *Perspectives of Fullerene Nanotechnology*, ed. E. Ōsawa, Springer, Netherlands, 2002, ch. 32, pp. 357–367.
6 B. S. Sherigara, W. Kutner and F. D'Souza, *Electroanalysis*, 2003, **15**, 753–772.
7 C. Brosseau, *Surf. Coat. Technol.*, 2011, **206**, 753–758.
8 M. J. Rosseinsky, *Chem. Mater.*, 1998, **10**, 2665–2685.
9 M. Riccò, T. Shiroka, M. Belli, D. Pontiroli, M. Pagliari, G. Ruani, D. Palles, S. Margadonna and M. Tomaselli, *Phys. Rev. B: Condens. Matter Mater. Phys.*, 2005, **72**, 155437.
10 V. N. Ivanova, *J. Struct. Chem.*, 2000, **41**, 135–148.
11 M. J. Rosseinsky, *J. Mater. Chem.*, 1995, **5**, 1497–1513.
12 T. Yildirim, O. Zhou and J. E. Fischer, in *The Physics of Fullerene-Based and Fullerene-Related Materials*, ed. W. Andreoni, Springer, Netherlands, 2000, vol. 23, ch. 2, pp. 23–66.
13 H. Nagashima, A. Nakaoka, Y. Saito, M. Kato, T. Kawanishi and K. Itoh, *J. Chem. Soc., Chem. Commun.*, 1992, 377–379.
14 K. Winkler, K. Noworyta, W. Kutner and A. L. Balch, *J. Electrochem. Soc.*, 2000, **147**, 2597–2603.
15 L. Norin, U. Jansson, C. Dyer, P. Jacobsson and S. McGinnis, *Chem. Mater.*, 1998, **10**, 1184–1190.
16 G. H. M. Dias, *Quim. Nova*, 1995, **18**, 592–596.
17 V. Lavrentiev, H. Abe, S. Yamamoto, H. Naramotoand and K. Narumi, *Mol. Cryst. Liq. Cryst.*, 2002, **386**, 139–143.
18 M. Wohlers, B. Herzog, T. Belz, A. Bauer, T. Braun, T. Rühle and R. Schlögl, *Synth. Met.*, 1996, **77**, 55–58.
19 A. V. Talyzin and U. Jansson, *Thin Solid Films*, 2003, **429**, 96–101.
20 A. S. Gurav, Z. Duan, L. Wang, M. J. Hampden-Smith and T. T. Kodas, *Chem. Mater.*, 1993, **5**, 214–216.
21 J. M. Cowley, M. Q. Liu, B. L. Ramakrishna, T. S. Peace, A. K. Wertsching and M. R. Pena, *Carbon*, 1994, **32**, 746–748.
22 A. V. Talyzin, A. Dzwilewski and M. Pudelko, *Carbon*, 2007, **45**, 2564–2569.
23 K. Winkler, K. Noworyta, A. de Bettencourt-Dias, J. W. Sobczak, C.-T. Wu, L.-C. Chen, W. Kutner and A. L. Balch, *J. Mater. Chem.*, 2003, **13**, 518–525.
24 T. Braun, M. Wohlers, T. Belz, G. Nowitzke, G. Wortmann, Y. Uchida, N. Pfänder and R. Schlögl, *Catal. Lett.*, 1997, **43**, 167–173.
25 V. Lavrentiev, H. Abe, H. Naramoto, S. Sakai and K. Narumi, *Chem. Phys. Lett.*, 2006, **424**, 101–104.
26 D. Östling and A. Rosén, *Chem. Phys. Lett.*, 1993, **202**, 389–393.
27 J. Roques, F. Calvo, F. Spiegelman and C. Mijoule, *Phys. Rev. B: Condens. Matter Mater. Phys.*, 2003, **68**, 205412.
28 J. Pitarch-Ruiz, S. Evangelisti and D. Maynau, *J. Mol. Struct.: THEOCHEM*, 2004, **681**, 203–207.
29 L. M. Ramaniah and M. Boero, *J. Chem. Phys.*, 2010, **133**, 134701.
30 A. N. Andriotis, M. Menon and G. E. Froudakis, *Phys. Rev. B: Condens. Matter Mater. Phys.*, 2000, **62**, 9867–9871.
31 A. N. Andriotis and M. Menon, *Phys. Rev. B: Condens. Matter Mater. Phys.*, 1999, **60**, 4521–4524.
32 M. K. Shukla, M. Dubey and J. Leszczynski, *ACS Nano*, 2008, **2**, 227–234.
33 Q. Zeng, X. Chu, M. Yang and D.-Y. Wu, *Chem. Phys.*, 2012, **395**, 82–86.
34 L. M. Ramaniah, M. Boero and M. Laghate, *Phys. Rev. B: Condens. Matter Mater. Phys.*, 2004, **70**, 035411.
35 M. Matsubara, C. Massobrio, L. M. Ramaniah, E. Ruiz and M. Boero, *Phys. Rev. B: Condens. Matter Mater. Phys.*, 2010, **81**, 195433.
36 O. Loboda, *Quantum-chemical studies on Porphyrins, Fullerenes and Carbon Nanostructures, Carbon Nanostructures*, Springer-Verlag Berlin, Heidelberg, 2013.
37 J. R. Kremer, D. N. Mastronarde and J. R. McIntosh, *J. Struct. Biol.*, 1996, **116**, 71–76.
38 C. MessaoudiI, T. Boudier, C. O. S. Sorzano and S. Marco, *BMC Bioinf.*, 2007, **8**, 288.
39 G. Kresse and J. Furthmüller, *Comput. Mater. Sci.*, 1996, **6**, 15–50.
40 G. Kresse and J. Hafner, *Phys. Rev. B: Condens. Matter Mater. Phys.*, 1993, **47**, 558–561.

41 G. Kresse and J. Furthmüller, *Phys. Rev. B: Condens. Matter Mater. Phys.*, 1996, **54**, 11169–11186.
42 G. Kresse and J. Hafner, *Phys. Rev. B: Condens. Matter Mater. Phys.*, 1994, **49**, 14251–14269.
43 P. E. Blöchl, *Phys. Rev. B: Condens. Matter Mater. Phys.*, 1994, **50**, 17953–17979.
44 G. Kresse and D. Joubert, *Phys. Rev. B: Condens. Matter Mater. Phys.*, 1999, **59**, 1758–1775.
45 J. P. Perdew, K. Burke and M. Ernzerhof, *Phys. Rev. Lett.*, 1996, **77**, 3865–3868.
46 M. Dion, H. Rydberg, E. Schröder, D. C. Langreth and B. I. Lundqvist, *Phys. Rev. Lett.*, 2004, **92**, 246401.
47 G. Román-Pérez and J. M. Soler, *Phys. Rev. Lett.*, 2009, **103**, 096102.
48 J. Klimeš, D. R. Bowler and A. Michaelides, *Phys. Rev. B: Condens. Matter Mater. Phys.*, 2011, **83**, 195131.
49 K. Jiří, R. B. David and M. Angelos, *J. Phys.: Condens. Matter*, 2010, **22**, 022201.
50 K. Momma and F. Izumi, *J. Appl. Crystallogr.*, 2011, **44**, 1272–1276.
51 C. Amiens, B. Chaudret, D. Ciuculescu-Pradines, V. Colliere, K. Fajerwerg, P. Fau, M. Kahn, A. Maisonnat, K. Soulantica and K. Philippot, *New J. Chem.*, 2013, **37**, 3374–3401.
52 C. Vauthier and K. Bouchemal, *Pharm. Res.*, 2009, **26**, 1025–1058.
53 C. Mabille, F. Leal-Calderon, J. Bibette and V. Schmitt, *Europhys. Lett.*, 2003, **61**, 708–714.
54 V. Schmitt, F. Leal-Calderon and J. Bibette, *Top. Curr. Chem.*, 2003, **227**, 195–215.
55 S. K. Smoukov, T. Tian, N. Vitchuli, S. Gangwal, P. Geisen, M. Wright, E. Shim, M. Marquez, J. Fowler and O. D. Velev, *Adv. Mater.*, 2015, **27**, 2642–2647.
56 *CRC Handbook of Chemistry and Physics*, ed. W. M. Haynes, CRC Press, 95th edn, 2014.
57 R. S. Ruoff, D. S. Tse, R. Malhotra and D. C. Lorents, *J. Phys. Chem.*, 1993, **97**, 3379–3383.
58 E. Grądzka, M. Wysocka-Żołopa and K. Winkler, *J. Phys. Chem. C*, 2014, **118**, 14061–14072.
59 M. R. Axet, O. Dechy-Cabaret, J. Durand, M. Gouygou and P. Serp, *Coord. Chem. Rev.*, 2016, **308**, 236–345.
60 P. J. Fagan, J. C. Calabrese and B. Malone, *Science*, 1991, **252**, 1160–1161.
61 H. Nagashima, Y. Kato, H. Yamaguchi, E. Kimura, T. Kawanishi, M. Kato, Y. Saito, M. Haga and K. Itoh, *Chem. Lett.*, 1994, **23**, 1207–1210.
62 A. A. Voityuk, *J. Phys. Chem. A*, 2009, **113**, 11801–11808.
63 Y. Huang and B. S. Freiser, *J. Am. Chem. Soc.*, 1991, **113**, 8186–8187.
64 A. D. Darwish, A. G. Avent, R. Taylor and D. R. M. Walton, *J. Chem. Soc., Perkin Trans. 2*, 1996, 2051–2054.
65 R. Bini, J. Ebenhoch, M. Fanti, P. W. Fowler, S. Leach, G. Orlandi, C. Ruchardt, J. P. B. Sandall and F. Zerbetto, *Chem. Phys.*, 1998, **232**, 75–94.
66 A. V. Talyzin, Y. O. Tsybin, T. M. Schaub, P. Mauron, Y. M. Shulga, A. Zuettel, B. Sundqvist and A. G. Marshall, *J. Phys. Chem. B*, 2005, **109**, 12742–12747.
67 A. V. Talyzin, Y. O. Tsybin, J. M. Purcell, T. M. Schaub, Y. M. Shulga, D. Noreus, T. Sato, A. Dzwilewski, B. Sundqvist and A. G. Marshall, *J. Phys. Chem. A*, 2006, **110**, 8528–8534.
68 R. Ghafouri and M. Anafcheh, *Fullerenes, Nanotubes, Carbon Nanostruct.*, 2015, **23**, 40–48.
69 S. M. C. Vieira, W. Ahmed, P. R. Birkett, C. A. Rego, S. Kotsiris and T. Drewello, *Fullerenes, Nanotubes, Carbon Nanostruct.*, 2004, **12**, 139–145.
70 T. Wagberg, D. Johnels, A. Peera, M. Hedenstroem, Y. M. Schulga, Y. O. Tsybin, J. M. Purcell, A. G. Marshall, D. Noreus, T. Sato and A. V. Talyzin, *Org. Lett.*, 2005, **7**, 5557–5560.
71 R. E. Haufler, J. Conceicao, L. P. F. Chibante, Y. Chai, N. E. Byrne, S. Flanagan, M. M. Haley, S. C. O'Brien, C. Pan, *et al.*, *J. Phys. Chem.*, 1990, **94**, 8634–8636.
72 A. S. Lobach, Y. M. Shul'ga, O. S. Roshchupkina, A. I. Rebrov, A. A. Perov, Y. G. Morozov, V. N. Spector and A. A. Ovchinnikov, *Fullerene Sci. Technol.*, 1998, **6**, 375–391.
73 S. M. Luzan, Y. O. Tsybin and A. V. Talyzin, *J. Phys. Chem. C*, 2011, **115**, 11484–11492.
74 A. V. Talyzin, Y. M. Shulga and A. Jacob, *Appl. Phys. A: Mater. Sci. Process.*, 2004, **78**, 1005–1010.
75 L. Becker, T. P. Evans and J. L. Bada, *J. Org. Chem.*, 1993, **58**, 7630–7631.
76 Y. M. Wuu, J. G. Bentsen, C. G. Brinkley and M. S. Wrighton, *Inorg. Chem.*, 1987, **26**, 530–540.
77 Y. M. Wuu, C. Zou and M. S. Wrighton, *Inorg. Chem.*, 1988, **27**, 3039–3044.
78 S. L. Ingham and S. W. Magennis, *J. Organomet. Chem.*, 1999, **574**, 302–310.
79 P. Lara, T. Ayvali, M.-J. Casanove, P. Lecante, A. Mayoral, P.-F. Fazzini, K. Philippot and B. Chaudret, *Dalton Trans.*, 2013, **42**, 372–382.
80 X. Qi, M. R. Axet, K. Philippot, P. Lecante and P. Serp, *Dalton Trans.*, 2014, **43**, 9283–9295.
81 S. J. Chase, W. S. Bacsa, M. G. Mitch, L. J. Pilione and J. S. Lannin, *Phys. Rev. B: Condens. Matter Mater. Phys.*, 1992, **46**, 7873–7877.
82 J. T. Miller, A. J. Kropf, Y. Zha, J. R. Regalbuto, L. Delannoy, C. Louis, E. Bus and J. A. van Bokhoven, *J. Catal.*, 2006, **240**, 222–234.

